Materials and Design 58 (2014) 346–356

Contents lists available at ScienceDirect

Materials and Design

journal homepage: www.elsevier.com/locate/matdes

Corrosion evaluation of multi-pass welded nickel–aluminum bronze alloy in 3.5% sodium chloride solution: A restorative application of gas tungsten arc welding process

Behnam Sabbaghzadeh [a], Reza Parvizi [a], Ali Davoodi [b,*], Mohammad Hadi Moayed [a]

[a] Department of Materials and Metallurgical Engineering, Faculty of Engineering, Ferdowsi University of Mashhad, 91775-1111, Iran
[b] Department of Materials and Polymer Engineering, Faculty of Engineering, Hakim Sabzevari University, Sabzevar 391, Iran

ARTICLE INFO

Article history:
Received 15 October 2013
Accepted 10 February 2014
Available online 18 February 2014

Keywords:
Gas tungsten arc welding
Nickel–aluminum bronze
Galvanic corrosion
EIS

ABSTRACT

In this research, the corrosion behavior of a gas tungsten arc welded nickel–aluminum bronze (NAB) alloy is investigated by DC and AC electrochemical techniques in 3.5% sodium chloride solution. Regarding the electrochemical impedance spectroscopy and potentiodynamic results, uniform corrosion resistance of instantly immersed weld and base samples are almost analogous and increased (more in weld region) during the immersion times. Moreover, zero resistant ammeter results demonstrated that the few nano-ampere galvanic currents are attributed to microstructural and morphological differences between these two regions. Therefore, the welding procedure could not deteriorate the general corrosion resistance of the restored damaged NAB parts operating in marine environments.

1. Introduction

Nickel–aluminum bronze (NAB) alloys containing 9–12% (wt.%) aluminum with additions of up to 6% (wt.%) of iron and nickel, represent one of the most important groups of commercial aluminum bronzes. As the major alloying element, aluminum content would result in higher strength and improve the corrosion resistance (by formation of an oxide/hydroxide film) and castings/hot working properties. On the other side, nickel also improves corrosion resistance, strength and stabilises the microstructure while iron refines grains and increases the alloy tensile strength [1,2]. Both cast and wrought aluminum bronze compounds offer a good combination of mechanical properties and corrosion resistance. Consequently, aluminum bronzes have been widely used for decades in a variety of marine or saline environments including valves, fittings, ship propellers, pump castings, pump shafts, valve stems and heat exchanger water boxes [2–4]. However, these alloys can suffer from localized corrosion (e.g. pitting, crevice, etc.) especially in flow conditions [5]. NAB alloys are metallurgical complex alloys with several intermetallic phases such as α, β', κ_i, κ_{ii}, κ_{iii} and κ_{iv} in which small variations in composition can result in development of markedly different microstructures. This can also lead to extensive changes of alloy corrosion resistance in seawater. The microstructures that can result in an optimum corrosion resistance can be obtained by controlling the composition and the heat treatment procedure [1]. Wharton et al. used five types of NAB alloys (as-cast and wrought) with different compositions and heat treatment (annealing) backgrounds and compared their corrosion behaviors through various electrochemical techniques [1]. They reported that the cast/annealed samples represented higher corrosion current densities in compared to wrought samples in seawater [1]. However, NABs are the most corrosion resistant types of copper-based alloys to flow-induced corrosion [5,6]. Their resistance has been attributed to a thin protective layer, containing aluminum and copper oxides [7,8]. Due to the presence of stable intermetallic compounds in NAB and the α/β phase boundary that is near the solidus line, it is very difficult to homogenize these alloys at their solid state and thus, a welding approach can be performed for this aim [9]. Indeed, this is a crucial matter whenever an inevitable industrial assembling process such as welding operation is carried out.

Alternatively, some defects and cracks can be induced by cavitation, de-alloying, stress corrosion cracking, pitting and erosion–corrosion mechanisms in some parts of NAB alloys (e.g. impellers), after long exposure times to seawater [10–14]. For instance, Alfantazi et al. reported that for a couple of copper alloys in 1 M NaCl solution (pH = 6), the samples experienced a general dissolution mechanism at higher overpotentials and did not suffer from localized corrosion while at more alkaline pH conditions, they revealed a type of passivity (and passivity breakdown) behavior in

* Corresponding author. Tel./fax: +98 5714003520.
E-mail address: a.davoodi@hsu.ac.ir (A. Davoodi).

http://dx.doi.org/10.1016/j.matdes.2014.02.019
0261-3069/

potentiodynamic results [2]. Also, Ni et al. showed that the NAB samples had finer and more homogenous microstructure (after performing a friction stir process) in comparison with the unprocessed alloy and that resulted in better corrosion resistance [15]. Furthermore, the namely materials can suffer surface damage under conditions of extreme flow velocity or fluid disturbance [5]. Since replacement of these parts with exactly the same material is very expensive, welding operation could be an economical method for restoration of NAB parts. Meanwhile, this method may lead to severe corrosion attacks due to occurrence of galvanic couples between weld and base alloy zones. However, there have been few studies committed to corrosion investigation of welded NAB alloys. For example, Ni et al. have employed the friction stir processing as a technique to modify the microstructure of the NAB alloys and have investigated the general corrosion properties of the surface processed NAB alloy [15]. Xiao-ya et al. also studied the cavitation behavior of NAB welds and showed that this type of corrosion initiates at the phase boundaries [16].

The aim of this research is devoted to assess the general and galvanic corrosion behavior of multi-pass gas tungsten arc (GTA) welded nickel–aluminum bronze (C95800) plates by DC and AC electrochemical techniques in aerated 3.5% (wt.%) sodium chloride solution. On the basis of ZRA measurement, a clear picture of the mechanism responsible for galvanic corrosion between the base and weld regions is presented. Finally, it will be inferred from the results whether this specified operation can be employed on the restored NAB alloys.

2. Materials and methods

Two as-cast NAB (C95800) plates were used as welding materials. The chemical composition (in wt.%) of the alloy was determined by quantometery method as 9.14% Al, 4.75% Ni, 3.1% Fe, 0.75% Mn and Cu as balance. U-shape groove of alloy plates with 10 mm in thickness and 100 mm in both length and width were joined using a multi-pass GTAW process. Argon gas, as shielding gas, was continuously purged during the four welding passes. The filler metal was ERCuNiAl that was chosen due to AWS A5.7 standard in the proposed nominal composition range (in wt.%) of 8.5–9.5% Al, 4–5.5% Ni, 3–5% Fe, 0.6–3.5% Mn, 0.1% Zn, 0.1% Si, 0.02% Pb, 0.5% of other elements and Cu as balance. The mean values of AC welding current and voltage were 220 A and 22 V, respectively. After completion of the welding operations, the weldments were cooled in air. Identical, in surface area, specimens with ca 0.203 cm^2 in cross section were extracted from the base and weld zones; see Fig. 1. Due to excessive conductivity of copper alloys and thus narrowness of the heat affected zone (HAZ), it was impossible to extract an individual sample from this zone. In order to examine the corrosion properties, the samples were cold mounted using a self-cure epoxy resin in cylindrical molds after an electrical connection was made between the sample and a copper wire. For corrosion and microstructural investigations, the samples were ground up to 1200 SiC abrasive paper, polished using 1 μm diamond paste, degreased by ethanol, washed by distilled water and finally dried by hot air. Prior to corrosion experiments, microstructural evaluations on individual parts of the prepared samples were performed using an Olympus optical microscopy (OM). The etchant used for metallographic examinations was prepared by mixing 8 g of ferric chloride, 25 ml of hydrochloric acid and 100 ml of distilled water in a glass beaker [17]. The corrosion properties of the base and weld regions were studied on individual samples by monitoring potentiodynamic polarization (PDP), electrochemical impedance spectroscopy (EIS) and zero resistant ammeter (ZRA). All corrosion experiments were done in aerated (exposed to air) 3.5 wt.% sodium chloride solution (prepared from distilled water and analytical Merck grade sodium chloride) with pH of 6.8 and at room temperature. Former to all corrosion measurements, each specimen was held at its rest potential for about 15 min to reach an stable corrosion potential. All electrochemical measurements were performed using an ACM instrument potentiostat (AC Gill No. 1380). A three electrode configuration was used for electrochemical measurements including platinum wire as the counter, saturated calomel as the reference and prepared specimens as the working electrodes, respectively. It should be noted that all potentials were measured and plotted against saturated calomel reference electrode (SCE). For PDP measurements, the potential was scanned from −400 to 1500 mV (vs. SCE) at 1 mV/s scanning rate. In order ot extract polarization parameters from PDP curves, Tafel extrapolation method was used. In order to study the galvanic couple (couple potentials and current densities) between these two identical (in surface area) samples (with 2–3 cm distance in between), zero resistant ammeter (ZRA) test was performed at 0, 24, 48 and 72 h of immersion. The galvanic current density (i_{couple}) and galvanic potential (E_{couple}) were recorded simultaneously as a function of time i.e. 900 s applying a zero potential against the galvanic cell. The current density was calculated by dividing the measured current to the area of the electrode. EIS test was also performed in the frequency range of 30,000–0.01 Hz with a potential amplitude of ±15 mV. The aim was to characterize and compare the surface evolution of instantly immersed (0 h) and 72 h immersed samples in three different applied overpotentials; 0 and ±100 mV (vs. SCE) with respect to each sample corrosion potential. The EIS results were analyzed and the equivalent circuits parameters were extracted by using the EIS spectrum analyzer software. Note that for checking the reproducibility of the electrochemical experiments, each of the corrosion tests was repeated for at least three times. Finally, the most representative data that was closest to the reported average values were selected for plotting.

3. Results and discussion

3.1. Microstructure characterization

Fig. 2 shows the microstructures and morphologies of the base and weld regions provided by OM. The image with lower magnification clearly reveals the sharp interface between these two regions (base and weld); see Fig. 2a. Base metal can be observed at the left

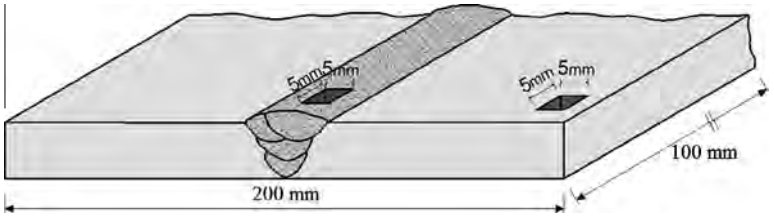

Fig. 1. Schematic illustration of the performed four-pass GTA welding procedure and the samples extraction sites from distinct base and weld regions.

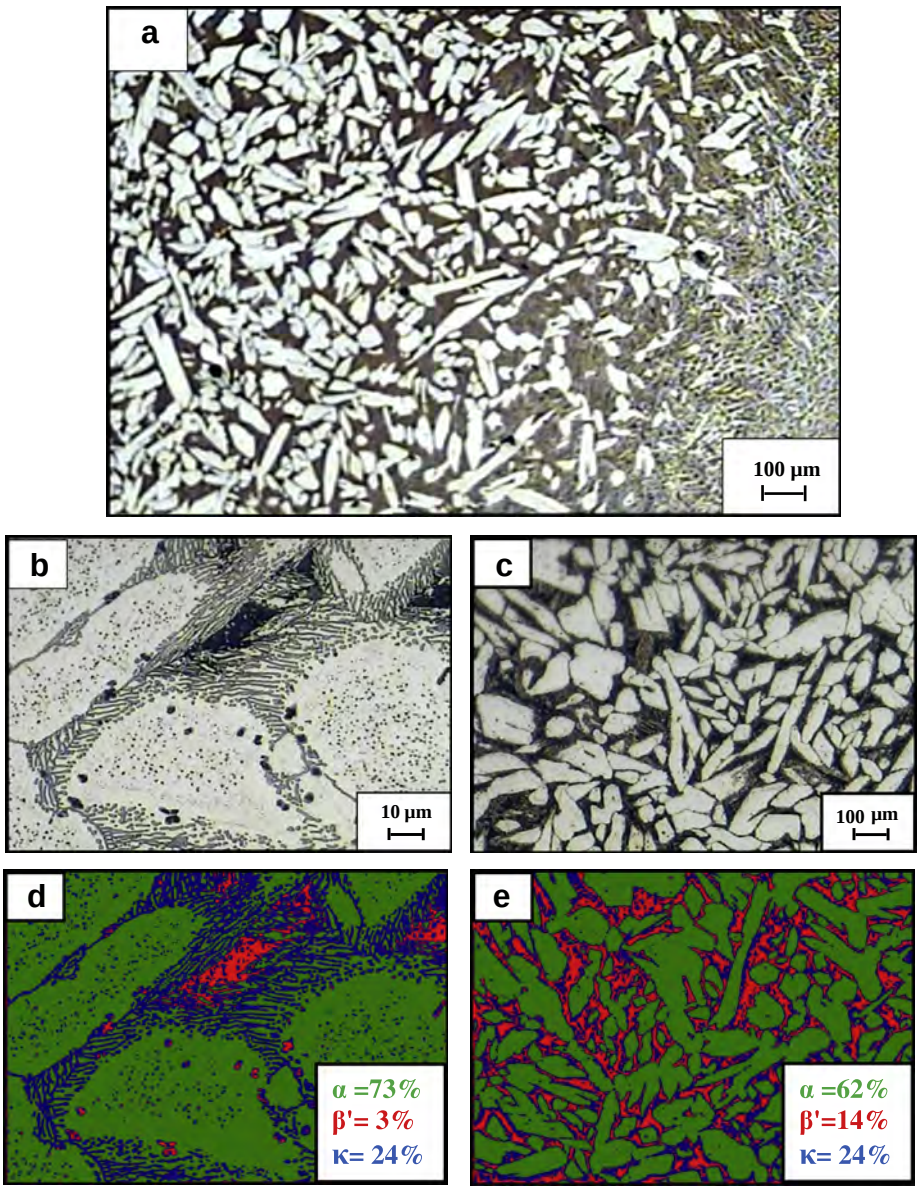

Fig. 2. Optical microscopy images taken from: (a) base/weld transition zone; (b) base and (c) weld regions. (d and e) are microstructurally analyzed images of figures (b and c), respectively.

side of the figure and in the right side, weld zone with smaller grain size is clearly apparent. A narrow transition zone with about 200 μm width, so called HAZ, could be observed as well. The microstructure of the NAB alloy in base region is shown in Fig. 2b. This region contains α phase as matrix (light color), which is a FCC copper-rich solid solution, β′ or retained β (darkest regions), also called as martensitic phase and several intermetallic phases such as κ_i, κ_{ii}, κ_{iii} and κ_{iv} [15]. Where, κ_i and κ_{ii} appear as large dendritic structures adjacent to α phase. Also, κ_{ii} is an iron-rich phase (based on Fe_3Al) which has the same dendritic structure, but its size is noticeably smaller than κ_i. Moreover, κ_{iii} is a nickel-rich phase (NiAl) and appears as a laminar eutectoid structure that coexists with α phase. Finally, κ_{iv} is an iron-rich phase, mostly appears as fine round particles embedded in matrix [1,16,18]. As can be seen, due to rapid solidification during welding operation, microstructural changes including significant grain refining and phase fraction modification in weld region occur; see Fig. 2c. Microstructural image processing (MIP) cleared that the volume phase fraction of β′ increases from 3% (±0.5%) in base metal to about 14% (±0.5%) in weld zone. Also, the phase fraction of α decreases from 73% (±0.5%) in base metal to about 62% (±0.5%) in weld zone and almost no change in the fraction of κ phase (including all types of κ phases) is identified; see Fig. 2d and e. This indicates that the cooling rate in welding operation is quite high that there is not enough time for decomposition of β to α (as can be achieved at equilibrium cooling rates in base metal). Due to decomposition of β to β′ instead of β to α, the volume fraction of β′ phase increases after the welding procedure. Fig. 3 shows an OM image of the HAZ zone representing some of its constituent phases. Where, α Widmanstatten forms from β phase (in the alloy equilibrium diagram) at a moderate to low cooling rate [19]. In this zone, the cooling rate is considered to be higher than the base metal (in casting condition) and lower than the weld zone, therefore, β phase could not decompose to α and consequently it decomposes to α Widmanstatten. Other constituent phases such as β′, κ_{iii}, κ_{iv} and α, are also evident in this figure.

3.2. Potentiodynamic polarization tests

Fig. 4a represents the PDP curves and Table 1 shows the extracted parameters of these results. For more clarity, higher

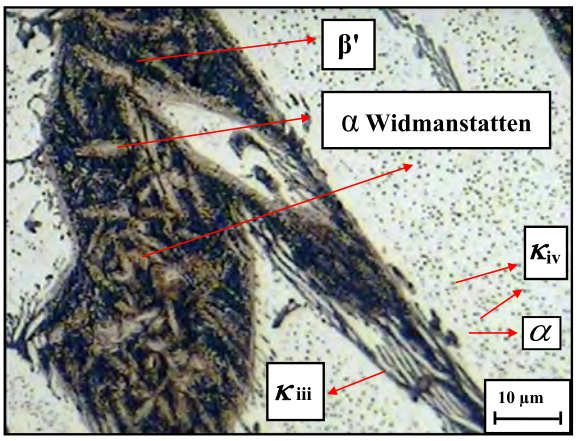

Fig. 3. Optical microscopy image taken from the heat affected zone (HAZ), revealing the Widmanstatten morphology of α phase.

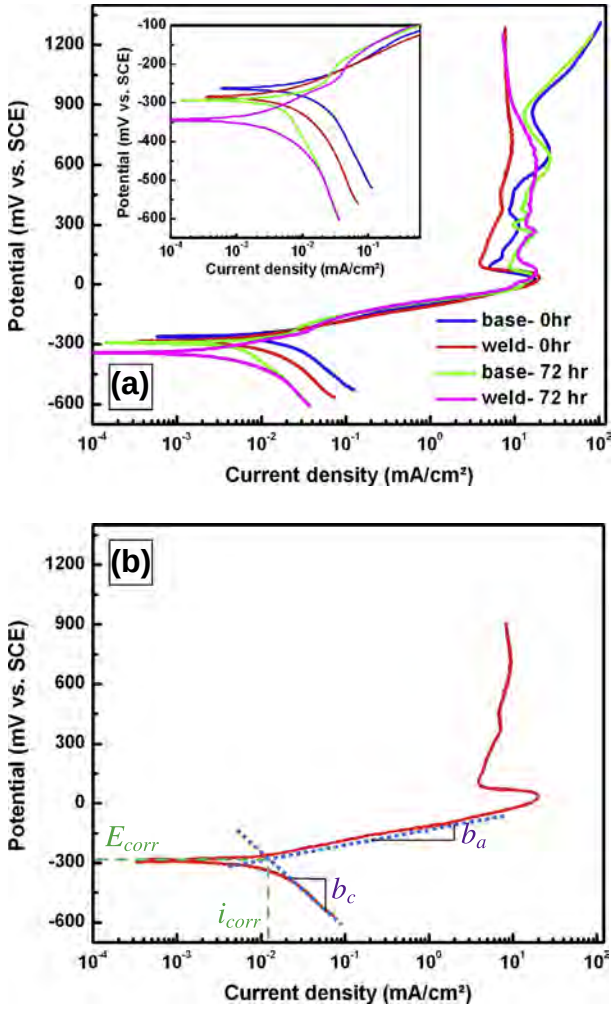

Fig. 4. (a) potentiodynamic polarization curves of the base and weld samples recorded after 0 and 72 h of immersion in aerated 3.5% sodium chloride solution and (b) schematic illustration of Tafel extrapolation fits to extract various parameters from potentiodynamic curves.

magnification of polarization curves at potentials around their E_{corr} is shown in the inserted figure. Moreover, a schematic illustration of the Tafel extrapolation fittings for extraction of various parameters from potentiodynamic curves is represented in Fig. 4b. Concerning Fig. 4, at low positive overpotentials, active dissolution of the alloy surface could be observed during the anodic polarization for both samples. In this potential region, apparent Tafel behavior can be observed where mixed charge transfer and mass transport controlling kinetics are usually assumed [5,6]. Corrosion current densities (i_{corr}) of the base and weld regions after initial immersion in solution (0 h) are approximately similar and after 72 h, i_{corr} decreases in about one decade in both regions. It seems that decreasing in i_{corr} is related to the cathodic surface activity. As can be seen in Fig. 4 and Table 1, there are no noticeable differences in anodic curves (including anodic Tafel slopes and limiting current densities) of 0 and 72 h immersed specimens. On the other side, the cathodic reaction is significantly polarized during 72 h of immersion. It is evident that after 72 h of immersion, there is a deviation from the anodic Tafel slope (or a small step in anodic branch) at around 100 mV (vs. SCE) overpotential with respect to the sample E_{corr}. This can be attributed to the unreduced part of the oxide layer (after cathodic polarization), which forms after longer exposure times [20]. However, by further increasing the overpotential, this film destroys and almost all the anodic branches depict the same behavior. In other words, the cathodic surface activity plays a major role in decrease of i_{corr}.

After 72 h, the corrosion current density of the weld sample (7 μA/cm^2) has a smaller value comparing with the base sample (9 μA/cm^2). This slight difference is associated to the more homogenized morphology and finer microstructure of the weld sample. Hence, the protective layer formed on this sample may be more homogeneous than the base sample. Ni et al. also reported that the finer microstructure of NAB alloys (after friction stir processing) resulted in a better corrosion resistance of the alloy [15].

By time elapsing, the air-formed copper oxides is believed to be gradually replaced by chloride containing complexes, whereas the nickel alloying element is assumed to be almost soluble and the aluminum alloying element is proposed to be in oxide/hydroxide state [1]. It is reported that in neutral chloride solutions, the main initial corrosion product of copper (after removal of air-formed oxides) is cuprous chloride, CuCl, which forms from the following reaction steps [21]:

$$Cu \rightarrow Cu^{+} + 1e^{-} \quad (1)$$

$$Cu^{+} + Cl^{-} \rightarrow CuCl \quad (2)$$

It was also proposed that the cuprous chloride reacts to produce cuprous oxide (cuprite) which is the main constituent of thick corrosion product layers [21]. The cuprous oxide generally oxidizes over longer exposure times to cupric hydroxide ($Cu(OH)_2$) and atacamite ($Cu_2(OH)_3Cl$) in chloride containing solution according to the following reactions [22–24]:

$$Cu_2O + 3H_2O \rightarrow 2Cu(OH)_2 + 2H^{+} + 2e^{-} \quad (3)$$

$$Cu_2O + 2H_2O + Cl^{-}, \rightarrow Cu_2(OH)_3Cl + H^{+} + 2e^{-} \quad (4)$$

If the chemical nature of scale formation is considered only as a function of oxygen supply, the sequence (from left to right) of the formed layers at longer immersion times is $CuCl/Cu_2O/Cu(OH)_2$–$CuO/Cu_2(OH)_3Cl$ [21]. It can be concluded that at higher chloride concentrations, copper chloride complexes form via the following reactions [23,25,26]:

$$Cu^{+} \xrightarrow{Cl^{-}} CuCl_2^{-} \xrightarrow{Cl^{-}} CuCl_3^{2-} \xrightarrow{Cl^{-}} CuCl_4^{3-} \quad (5)$$

In copper alloys, it is well established [1,6,15,27] that the major corrosion process of the NAB alloys is the anodic dissolution of copper to form the cuprous dichloride anion simplified as:

$$Cu + 2Cl^{-} \rightarrow CuCl_2^{-} + e^{-} \quad (6)$$

Table 1
Potentiodynamic polarization parameters of the base and weld specimens after different immersion times (0 and 72 h) in aerated 3.5% sodium chloride solution. The represented data are the average of at least three experimental results; errors shown in the brackets are standard deviations.

Sample	Immersion time (hour)	b_a (mV dec^{-1})	b_c (mV dec^{-1})	i_{corr} (mA/cm^2)	E_{corr} (mV vs. SCE)
Base	0 h	78 (±4)	−355 (±5)	0.02 (±0.001)	−258 (±10)
	72 h	68 (±4)	−435 (±5)	0.009 (±0.002)	−298 (±5)
Weld	0 h	80 (±4)	−381 (±5)	0.021 (±0.004)	−285 (±15)
	72 h	71 (±4)	−450 (±5)	0.007 (±0.002)	−343 (±10)

The method of cuprous oxide formation (or in the inverse condition air-formed oxide dissolution) in presence of chloride ions is usually taken as a precipitation reaction rather than a direct electrochemical or chemical formation from the base metal or cuprous chloride as following [24,28,29]:

$$2CuCl_2^- + 2OH^- \leftrightarrow Cu_2O + H_2O + 4Cl^- \quad (7)$$

or alternatively, the CuCl produced by precipitation of dissolved Cu(I) in a chloride media may lead to further Cu_2O formation and growth [29]:

$$2CuCl + H_2O \leftrightarrow Cu_2O + 2H^+ + 2Cl^- \quad (8)$$

On the other hand, the stability of Cu_2O or its redissolution is inversely dependent on the concentration of chloride ions [21].

The apparent Tafel region of copper and copper alloys is limited by a peak current at around 10 mV (vs. SCE), which is associated to the CuCl formation [32,5]. It starts when the activity of $CuCl_2^-$ in the outer Helmholtz plane exceeds the solubility equilibrium due to the following reaction [20,25,30]:

$$CuC1 + C1^- \rightarrow CuC1_2^- \quad (9)$$

At higher overpotentials (after the current density peak), a subsequent film dissolution is observed giving a limiting current density, above that any increase in current density is due to the formation of Cu(II) species [7,23]. The cathodic reaction in base and weld samples in an aerated solution is mainly oxygen reduction reaction [31–34]:

$$O_2 + 2H_2O + 4e^- \rightarrow 4OH^- \quad (10)$$

By initially immersing the specimens in solution, the only film, which could be present at the surface, is the air-formed oxide layer. While by time elapsing, porous corrosion products constituted of chloride and oxide containing complexes, form and act as a barrier on the surface [7,35–37]. By formation of this layer, the diffusion rate of cathodic reaction species is restricted and consequently the cathodic current densities are decreased. This is due to the interaction between reaction species and the corrosion products in porosities.

By considering the cathodic branches of polarization curves (see Fig. 4 and Table 1), it seems that the cathodic reaction is under diffusion limited control condition. Indeed, it is found that the cathodic characteristics of polarization curves are strongly dependent on the immersion time prior to polarization [1,6]. It has been reported that at initial immersion times, reduction of CuCl influences the oxygen reduction reaction while at higher immersion times; the former reaction is mainly affected by reduction of the formed Cu_2O species [6,7]. Moreover, it was proposed by some authors that during the cathodic polarization of copper, an underlying layer of cuprous species will be initially reduced followed by immediate reduction of overlying cupric species at higher overpotentials [6,7]. This will complicate the overall oxygen reduction mechanism. The substrate, temperature, surface and electrolyte conditions can all affect the reduction mechanisms. Therefore, the oxygen reduction reaction can be taken place under charge transfer/kinetic, mass-transfer or even mixed mass and charge transfer control [6].

In summary, the corrosion rates at corrosion potentials are quite low due to low rate of reduction reactions (predominately-dissolved oxygen). Since the corrosion behavior of this alloy in under cathodic control, the corrosion potential does not increase with time but rather decreases with time because of more polarization of the cathodic reaction [6]. That is the reason for employing these types of alloys in marine environments (considering the sharp increase in anodic current densities at anodic overpotentials). In this study, in both base and weld specimens, their corrosion potentials (at initial immersion times) are decreased about 50 mV after 72 h of immersion. More details on surface layer characterization will be discussed later by EIS results in the next section.

3.3. Electrochemical impedance spectroscopy results

In order to characterize the uniform corrosion behavior of the two distinct regions and also to authenticate the PDP results, the EIS technique was employed on each sample. Figs. 5–7 show Nyquist and Bode plots of the base and weld samples at their E_{corr} and at ±100 mV overpotentials (with respect to their E_{corr}) after 0 and 72 h of immersion. The solid lines in these figures show simulated curves which are obtained by EIS spectrum analyzer while, the symbolic plots represent the real experimental data. According to the EIS results, two possible types of equivalent circuits could be proposed for the surface reactions response. This is most likely due to complex reactions that can occur on the surface in presence of Cl^- ions, particularly since Cu, Al and Ni elements are present in the alloy matrix [24,31,38–47]. Fig. 8a and b show the proposed equivalent circuits for extraction of EIS data considering a porous corrosion product film. Moreover, based on the extracted C an n values from the EIS results, the schematic images depict the base and weld samples (maintained at their E_{corr} and E_{corr} ± 100 mV) surface evolution (variations in surface roughness, film thickness) during 72 h of immersion in aerated 3.5% NaCl solution; see Fig. 8c–e.

The obtained Nyquist and Bode curves at E_{corr} in Fig. 5 consist of a double-loop Randle-like semicircle in two parts; a high frequency impedance arc (related to charge transfer resistance) and a low frequency impedance arc (related to protective surface layer or film resistance). The equivalent circuits generally contain R_s (Ω cm^2) as the solution resistance, R_{ct} (Ω cm^2) as the charge transfer resistance (also known as polarization resistance) at the alloy/electrolyte interface, CPE_{ct} (μF/cm^2) as the non-ideal capacitance of charge transfer, R_f (Ω cm^2) as the surface film resistance, CPE_f (μF/cm^2) as the non-ideal capacitance of surface film and W (Ω/s$^{0.5}$) as the Warburg element. The constant phase element, CPE (μF/cm^2), is expressed in the form of $P(i\omega)^n$ in which P (μF/cm^2) is related to the capacitance, n is a parameter related to surface roughness, and ω (rad/s) is the angular frequency [48,49]. Applying CPE (a leaking capacitance) instead of pure capacitance improves EIS data fitting of the experimental results. In order to evaluate the corrosion product layer, the CPE values should be correlated to the capacitance (C) values. One of the most acceptable equations for calculation of capacitance from CPE values is the following [49]:

$$C = \sqrt[n]{P(R_P)^{1-n}} \quad (11)$$

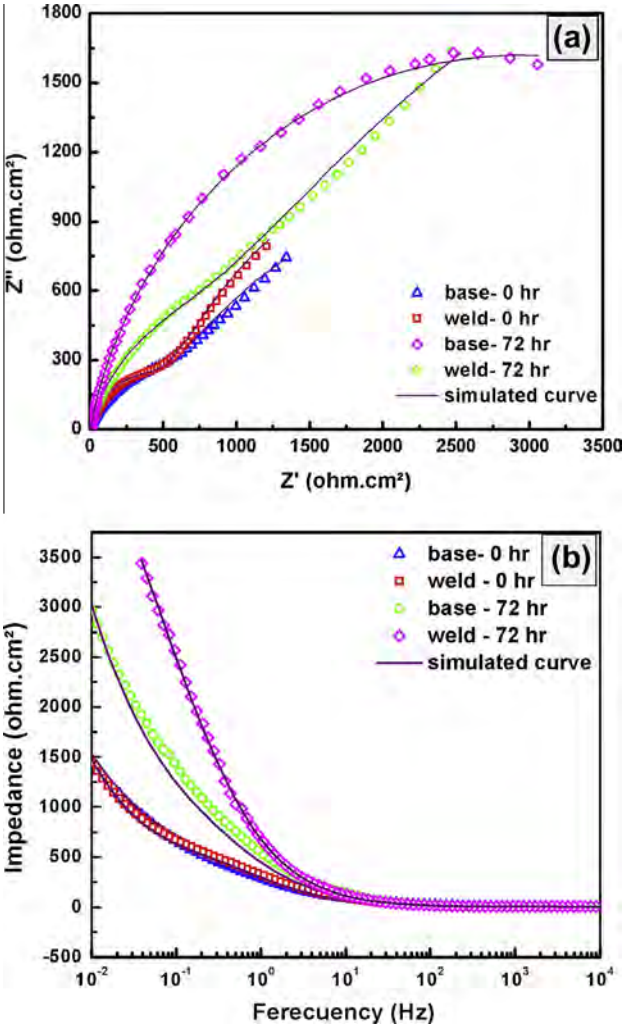

Fig. 5. (a) Nyquist plots and (b) Bode plots of the base and weld samples at their E_{corr} (mV vs. SCE) after 0 and 72 h immersion in aerated 3.5% sodium chloride solution. The proposed equivalent circuit used to fit/simulate and extract the parameters of these plots is included as an inserted figure in the Bode plot.

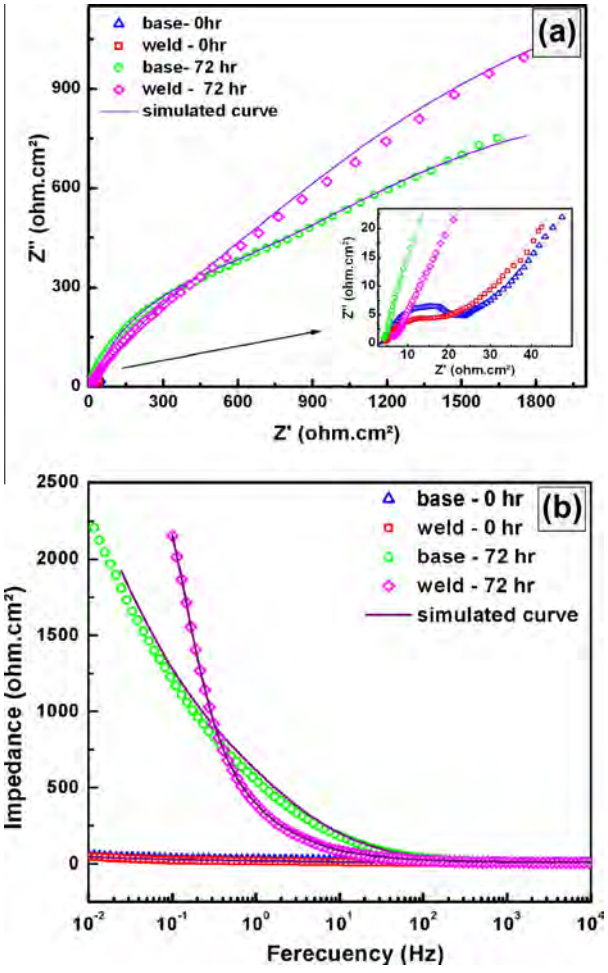

Fig. 6. (a) Nyquist plots and (b) Bode plots of the base and weld samples at 100 mV above their E_{corr} (mV vs. SCE) after 0 and 72 h immersion in aerated 3.5% sodium chloride solution. The proposed equivalent circuits for the base and weld samples after 0 (containing Warburg element) and 72 h of immersion are included as inserted figures in the Bode plot.

Moreover, it is well known that the capacitance is inversely proportional to the surface film thickness according to following equation [42,49]:

$$C = \frac{\varepsilon_o \varepsilon}{d} S \tag{12}$$

where d (cm) is the thickness of the surface film (e.g. double layer thickness), S (cm^2) is the surface of the electrode (or the active surface area), ε_o (μF/cm) is the permittivity of air and ε is the local dielectric constant. While ε_o, ε and S are assumed to be constant in all experiments, variations in C values are an indication of surface layer thickening/thinning process (C is inversely correlated to d). Extracted and calculated values obtained from equivalent circuits (as described in Figs. 5–7) are listed in Tables 2 and 3.

In Fig. 5, the recorded corrosion potentials of the base sample at 0 and 72 h were −243 and −265 mV (vs. SCE), respectively, while for the weld sample they were −255 and −296 mV (vs. SCE), respectively. It is obvious that the general difference observed between the base and weld samples at 0 h curves is insignificant. From Table 2, in both regions and at E_{corr}, the surface film resistance (R_f) is around five times higher than the charge transfer resistance (R_{ct}) which is in agreement with literature [22,39,41,47]. This means that the formed surface layer on the C95800 alloys can play a considerable role on their corrosion resistance. This layer is aluminum-rich adjacent to the base metal and richer in copper in the outer regions, see Fig. 8 [1,4,15,27].

Moreover, since n_f values of the weld region at 0 h (0.72) is higher than the base (0.60), it gives a more uniform surface layer with slightly higher thickness (comparing the capacitance values of 0.015 F/cm^2 and 0.020 F/cm^2 for the weld and base samples, respectively). This can be attributed to more homogenized microstructure of the weld region, see Figs. 2 and 8.

Comparing the results of Fig. 5 and Tables 2 and 3, it is obvious that the semicircles diameters and thus, the values of R_{ct} and R_f (particularly surface film resistance) are enhanced by increasing in the exposure time from 0 to 72 h. By comparing the curves, it can be inferred that at longer immersion times, only one semicircle appears. This is due to formation of double layer in surface layer porosities (typically at the bottom of diffusion paths). While the double layer can be formed at various sites (e.g. upon a dense surface layer or in diffusion paths), the elicited charge transfer parameters cannot be scientifically analyzed. Also, it is noticeable that the values of C_f for both samples are diminished, revealing that the layers thicknesses are increased in accordance; see Fig. 8. This means that by increasing in immersion time, the protective surface film, which acts as a corrosion barrier, grows and hence, slows down the general surface dissolution reactions. Moreover, the value of surface film resistance (R_f) in the weld sample is greater

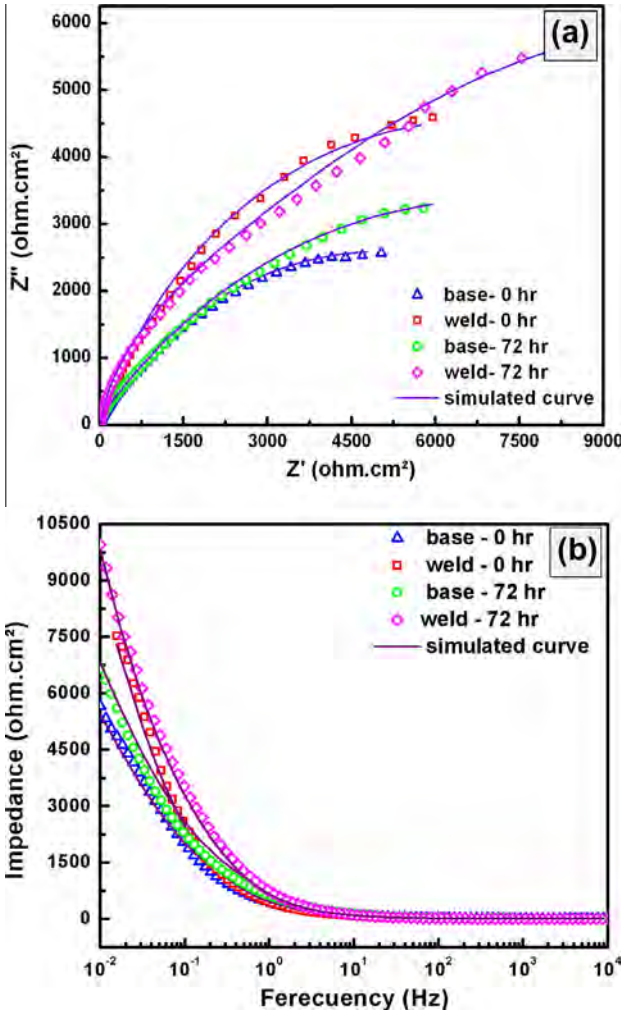

Fig. 7. (a) Nyquist plots and (b) Bode plots of the base and weld samples at 100 mV below their E_{corr} (mV vs. SCE) after 0 and 72 h immersion in aerated 3.5% sodium chloride solution. The proposed equivalent circuit used to fit/simulate and extract the parameters of these plots is included as an inserted figure in the Bode plot.

than that for the base sample i.e., 10,000 and 6500 $\Omega\,cm^2$, respectively. This result is suitably in agreement with i_{corr} results obtained from PDP measurements. Furthermore, by comparing the C_f and n_f values of the two regions (see Table 3) it can be deduced that the higher n_f value of the weld is related to its lower roughness (more homogenized microstructure) while its thickness is also lower; see Fig. 8. Indeed, it can be concluded that the corrosion product layer formed on the weld sample is denser in compared to the base. In addition, due to the n_f values of base and weld, it should be mentioned that the surface layers follow the Warburg behavior. This can be related to surface layer porosities that act as diffusion-controlling submicron paths or even the nature of the anodic controlling reactions [39,41].

In order to investigate the effect of anodic and cathodic polarizations on the film stability behavior, ±100 mV overpotentials were applied to the samples. Prior to apply these overpotentials, E_{corr} values of the electrodes (base and weld samples at various immersion times) were recorded against the reference electrode. In Figs. 6 and 7, (in both polarized conditions) the recorded E_{corr} values of the base sample at 0 and 72 h were around −240 and −270 mV (vs. SCE), respectively, while for the weld sample they were about −264 and −305 mV (vs. SCE), respectively.

At 0 h immersion, applying a 100 mV anodic overpotential leads to a remarkable decrease in R_{ct} and R_f values (also an increase in C_f values) and appearance of a Warburg element (in comparison with E_{corr} results); as can be observed in Fig. 6. This indicates that at this potential, the thin surface layer, to a greater extent, is uniformly dissolved and thus, the exposed bare surface does not exhibit a complete barrier characteristic. The Warburg element is believed to be related to the anodic mixed controlled reactions, e.g. dissolution reactions of copper to copper complexes such as $CuCl_2^-$ [2,39]. In summary, both regions revealed almost similar behaviors at 100 mV anodic potentials after initial immersion. This may be due to the active dissolution of surface constituents.

After 72 h of immersion, by applying a 100 mV anodic overpotential, the C_f and n_f values of both samples decreased (i.e. a considerable decrease in their surface layer thickness and homogeneity) while the R_f values increased comparing with 0 h results. This can be attributed to the formation of a more resistant and a thicker surface layer (smaller C_f values) with higher density of porosities (smaller n_f values) that affects the diffusion of the reaction species through them; see Fig. 8 (submicron paths). In other words, since at this potential the anodic curve is under mixed (diffusion and activation) control [2], and the values of n_f for both samples decreased, it can be stated that the surface layer has lost its uniformity and acts as a diffusion layer, in which the anodic reactions occur in porosities present at this layer. Comparing the 72 h results at the 100 mV anodic overpotential and at E_{corr} (Figs. 5 and 6 and Table 3), it can be observed that R_f values decreased regarding to higher kinetics of dissolution at this overpotential. Furthermore, while the C_f values are increased during the anodic polarization, the n_f values has not varied considerably. This in accordance with previous descriptions can be attributed to higher anodic dissolution rates.

Contrarily, considering Fig. 7 and Table 2, applying a 100 mV cathodic potential (at 0 h immersion) leads to a noticeable increase in the R_f values, particularly about four times higher than R_f values recorded at E_{corr}. On the other hand, it can be seen that the C_f and n_f values of the both samples are decreased (compared to E_{corr} results) as a result of the cathodic polarization, hence, a layer with higher thickness and roughness is formed on the surface; see Fig. 8. While the surface consists of a thin layer of corrosion products at instant immersion times, this phenomenon can be attributed to a non-uniform copper redeposition (formation of copper-deposited islands) during the cathodic polarization.

After 72 h of immersion, R_f, C_f and n_f values of both specimens are increased in compared to E_{corr} results (Figs. 5 and 7 and Table 3). This reveals that during the cathodic polarization, the corrosion product layer partially dissolves (an increase in C_f value and a decrease in the layer thickness) and the reduced copper, redeposits in porosities and results in an increase in the surface homogeneity (an increase in n_f values). Moreover, by copper redeposition, the open porosities are blocked and thus the rates of reactions (the diffusion of reaction species) are slowed down (an increase in R_f values).

From Fig. 7 and Tables 2 and 3, it can be clearly observed that the R_f values are increased by increasing in immersion time (from 0 to 72 h). On the other side, while the C_f values are diminished after 72 h, n_f values are almost unchanged. This fact in accordance with previous results is an indication for the thickening process of the surface layer by time elapsing; see Fig. 8. Moreover, it can be deduced that the surface homogeneity in compared to 0 h results is most likely remained unaffected. This is due to the copper redeposition process during the cathodic polarization at both immersion times. Since the surface layer is the main reason for the corrosion resistance in C95800 alloys, it is found that the exposure time, has a great effect on the cathodic reaction(s) (comparing with anodic reactions) and in this manner, it results in a decrease in the corrosion current densities.

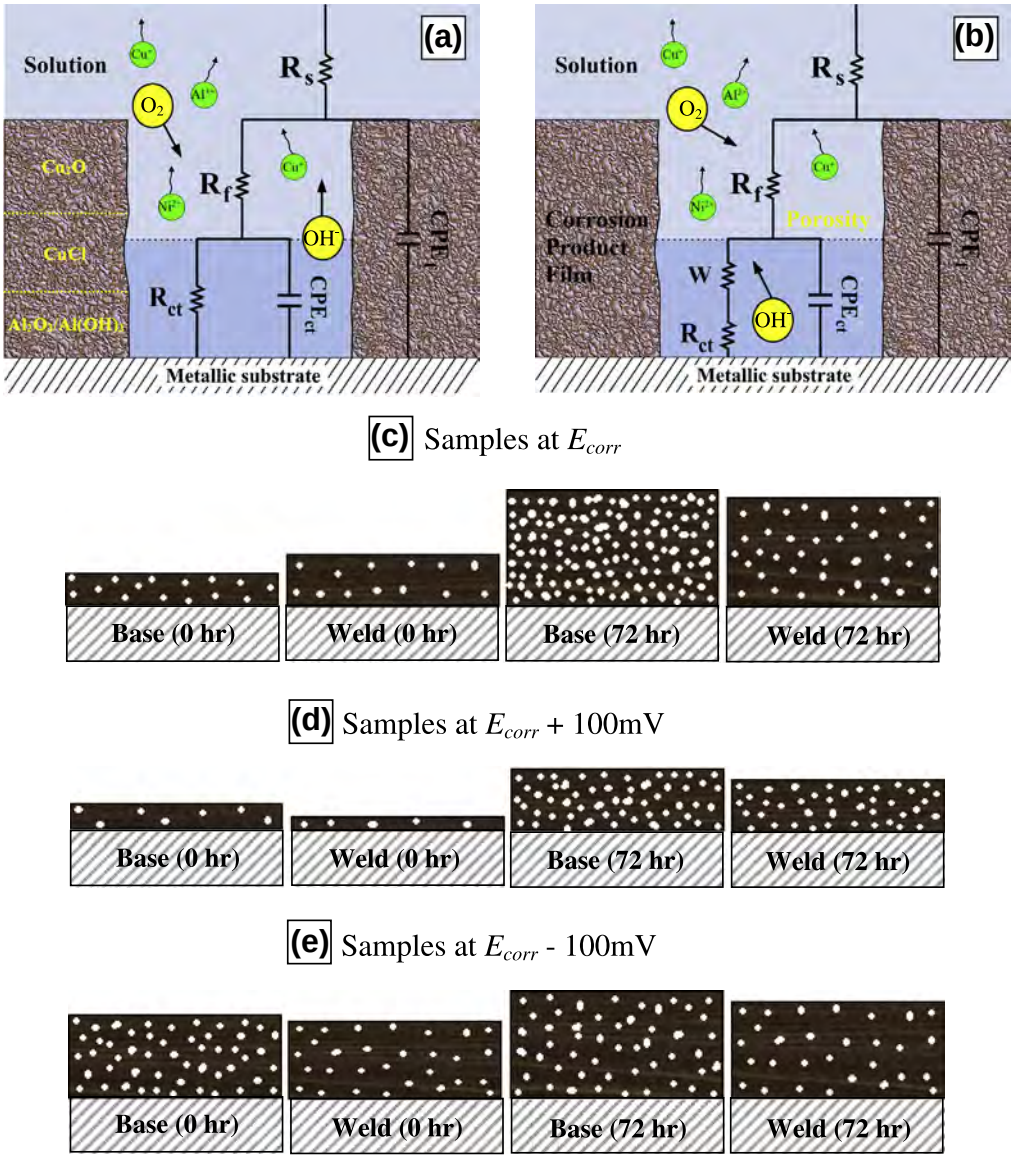

Fig. 8. (a and b) show the proposed equivalent circuits for extraction of EIS data considering a porous corrosion product film. (c–e) are schematic images depicting the surface layer evolution (based on extracted *C* an *n* values from EIS results) of the base and weld samples during 72 h immersion in aerated 3.5% NaCl solution. (c) For samples at their E_{corr}, (d) for samples at their E_{corr} + 100 mV and (e) for samples at their E_{corr} − 100 mV. The brownish layer is assumed to be the product film and the white spots are the porosities.

Table 2
Extracted EIS parameters (at E_{corr} and E_{corr} ± 100 mV) of the base and weld specimens after initial immersion in aerated 3.5% sodium chloride solution. The represented data are the average of at least three experimental results; errors shown in the brackets are standard deviations.

Sample	Potential (mV/SCE)	R_s (Ω cm^2)	R_{ct} (Ω cm^2)	R_f (Ω cm^2)	A_W (Ω/s$^{0.5}$)	n_{ct}	n_f	p_{ct} (μF/cm^2)	p_f (μF/cm^2)	C_{ct} (μF/cm^2)	C_f (μF/cm^2)
Base	E_{corr} − 100	4 (±1)	830 (±20)	9500 (±150)	–	0.80 (±0.02)	0.52 (±0.02)	300 (±10)	400 (±20)	230 (±10)	1500 (±100)
	E_{corr}	4.7 (±1)	650 (±10)	3500 (±200)	–	0.68 (±0.02)	0.60 (±0.04)	500 (±30)	3400 (±250)	360 (±30)	20,000 (±450)
	E_{corr} + 100	4 (±0.5)	20 (±2)	8 (±1)	5.7 (±0.5)	0.73 (±0.01)	0.87 (±0.02)	20,000 (±400)	48,000 (±300)	570 (±45)	40,000 (±600)
Weld	E_{corr} − 100	4 (±1)	1350 (±80)	12,000 (±300)	–	0.80 (±0.02)	0.63 (±0.03)	400 (±50)	100 (±15)	380 (±40)	1700 (±50)
	E_{corr}	4 (±1)	610 (±30)	3300 (±100)	–	0.75 (±0.02)	0.72 (±0.01)	500 (±40)	5200 (±100)	380 (±30)	15,000 (±400)
	E_{corr} + 100	4.1 (±1)	19 (±3)	9 (±2)	5.8 (±0.3)	0.57 (±0.01)	0.84 (±0.03)	6600 (±200)	72,000 (±400)	1500 (±100)	60,000 (±1400)

Table 3
Extracted EIS parameters (at E_{corr} and E_{corr} ± 100 mV) of the base and weld specimens after 72 h immersion in aerated 3.5% sodium chloride solution. The represented data are the average of at least three experimental results; errors shown in the brackets are standard deviations.

Sample	Potential (mV/SCE)	R_s (Ω cm^2)	R_{ct} (Ω cm^2)	R_f (Ω cm^2)	n_{ct}	n_f	p_{ct} (μF/cm^2)	p_f (μF/cm^2)	C_{ct} (μF/cm^2)	C_f (μF/cm^2)
Base	E_{corr} − 100	4.5 (±0.5)	500 (±50)	12,500 (±300)	0.85 (±0.03)	0.54 (±0.01)	200 (±20)	380 (±30)	100 (±10)	1100 (±15)
	E_{corr}	5.5 (±0.5)	1300 (±100)	6500 (±100)	0.83 (±0.03)	0.36 (±0.01)	300 (±10)	300 (±20)	220 (±10)	1000 (±25)
	E_{corr} + 100	5 (±1)	800 (±40)	3000 (±150)	0.75 (±0.01)	0.43 (±0.01)	200 (±10)	1700 (±70)	140 (±15)	5200 (±50)
Weld	E_{corr} − 100	6 (±1)	4400 (±200)	17,500 (±400)	0.87 (±0.02)	0.62 (±0.03)	300 (±30)	500 (±30)	310 (±25)	1400 (±30)
	E_{corr}	5.5 (±1)	1100 (±50)	10,000 (±200)	0.78 (±0.01)	0.56 (±0.02)	400 (±20)	1400 (±40)	320 (±10)	1100 (±20)
	E_{corr} + 100	6 (±0.5)	700 (±20)	4500 (±100)	0.65 (±0.01)	0.52 (±0.01)	100 (±10)	400 (±10)	230 (±10)	6800 (±80)

To sum up, the EIS in conjunction with DC results discloses that the uniform corrosion resistance of the alloy in aerated 3.5% sodium chloride solution in heat affected (weld) and unaffected (base) regions is improved by increasing in immersion time. In addition, it can be observed that the better homogeneity of the weld region results in a slightly better corrosion resistance of this zone almost at all polarization conditions.

3.4. Zero resistance ammeter results

The galvanic current and potential measured by ZRA method for the galvanic couples of base/weld are presented in Fig. 9. Due to higher corrosion potential of the base sample in compared to the weld sample, E_{corr} values in Table 1, base metal acts as the cathode and weld zone acts as the anode in the galvanic cell. During the first 900 s of immersion, the mean value of galvanic current (I_{couple}) is 0.75 nA. By time elapsing, the mean values of I_{couple} increases to about 0.93 nA after 24 h, then it decreases to around 0.06 nA in 48 h, and finally reaches to 2.95 nA after 72 h of exposure time. Considering the couple potentials (E_{couple}) presented in Fig. 9b, it can be seen that the mean values of the E_{couple} are −248, −234, −281 and −260 mV (vs. SCE) for 0, 24, 48 and 72 h of immersion, respectively. While the I_{couple} values are of few nanoamperes magnitudes, it seems that there is not such a considerable electrochemical difference between the base and weld zones during the whole immersion times; see Fig. 9. This means that the welding procedure could not result in the formation of a destructive galvanic couple between these two zones.

Taking into account the welding operation, induced microstructural and morphological changes in weld zone comparing with base sample are as follows: a decrease in α phase, an increasing in β′ phase and almost no changes in κ phase volume fractions. Although, the character of the phases may be altered because of the welding procedure, see Fig. 2. To differentiate the microstructural and morphological modifications, an additional superscript (α_w, β'_w and κ_w shown in Fig. 10) was used for individual phases in the weld region. The difference between volume fractions of the constituent phases most likely plays the major role in anodic and cathodic behaviors of these zones. To better identify the corrosion behavior of the constituent phases, phase fraction calculations were performed for both regions. For this couple, the anode (weld sample) is composed of 62 vol.% α_w, 24 vol.% κ_w and 14 vol.% β'_w (all with ± 0.5% deviation), while the cathode (base sample) is composed of 73 vol.% α, 24 vol.% κ and 3 vol.% β′ (all with ±0.5% deviation); see Fig. 2d and e. For this couple, according to the same volume fractions of κ and κ_w in both regions, it could also be assumed that these phases do not act as corrosion rate determining

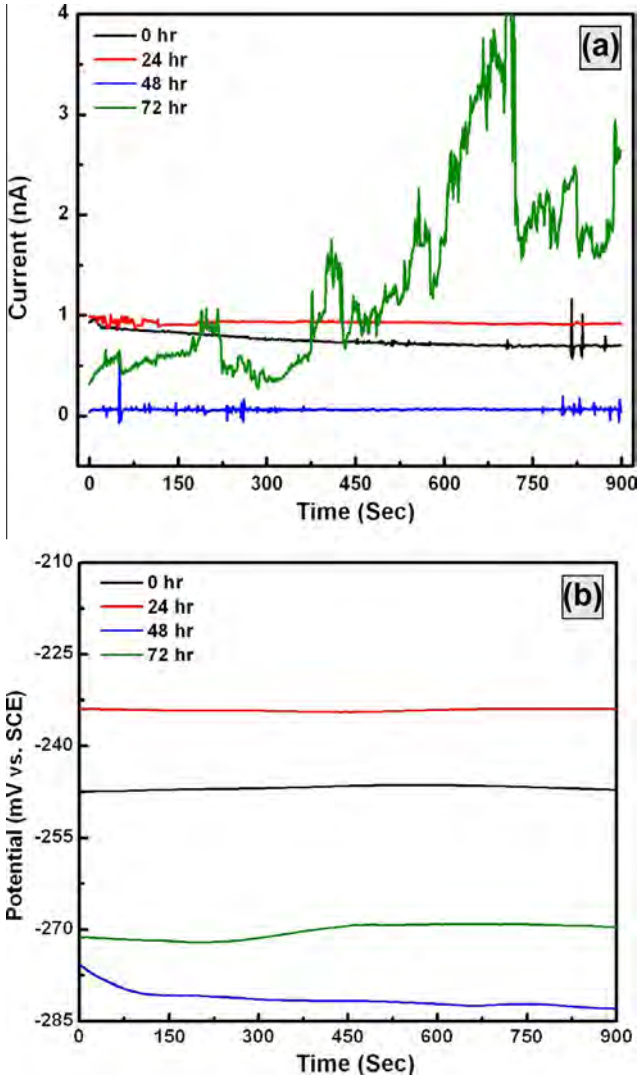

Fig. 9. Galvanic measurements between base and weld samples after 0, 24, 48 and 72 h of immersion in aerated 3.5% sodium chloride solution; (a) couple current (nA); and (b) couple potential (mV vs. SCE).

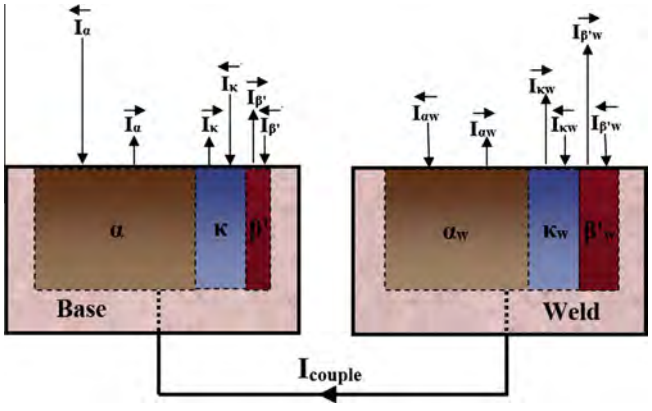

Fig. 10. Descriptive galvanic model representing the anodic and cathodic currents on each of the base and weld surface constituent phases. The arrow length is assumed to be an indication of current magnitudes.

phases in the proposed galvanic couple. In other words, it is assumed that the κ phase reveals anodic behavior on the anode (κ_w) and cathodic behavior on the cathode (κ). Due to higher volume fractions of β'_w phase in the weld sample; this can be accounted as the most important cause of the anodic behavior in this sample. In contrast, the volume fraction of α phase in base sample is higher than the weld (α_w) and therefore, it can be responsible for the cathodic behavior of the base specimen. Additionally, it was reported that the corrosion resistance of α phase is superior to β′ phase [13] and hence, it can be assumed that β′ (also β'_w in weld) phase behaves anodic at both the anode (weld) and the cathode (base) with similar anodic current densities, i_a. Moreover, α (also α_w in weld) phase in these samples plays mainly a cathodic behavior (oxygen reduction reaction takes place on its surface) with similar cathodic current densities, i_c [50].

To better understand the origin of overall current (I_{couple}) measured in ZRA method, a schematic illustration of the galvanic couple is presented in Fig. 10. Such an approach has been previously employed to express the effect of Cu-rich phases on galvanic corrosion of aluminum–copper model alloys [50]. In Fig. 10, the length of the current vectors is a criterion of their magnitude. To elucidate the proposed model at galvanic potential, sum of the anodic and cathodic currents should be equal according to the following equation:

$$\sum \overrightarrow{I}_a = \sum \overleftarrow{I}_c \tag{13}$$

where $\sum \overrightarrow{I}_a$ is sum of anodic currents and $\sum \overleftarrow{I}_c$ is sum of cathodic currents generated/consumed from the individual phases, which are present in each of the base and the weld samples. To simplify the galvanic model, the anodic and the cathodic currents with lower values (small current magnitudes illustrated by vectors in Fig. 10) are assumed to be negligible. In other words, although α (α_w) demonstrates a cathodic behavior in both samples, its elicited anodic currents in base and weld samples are insignificant. Also, it is assumed that the κ phase in base sample acts as a cathode while it (κ_w) inversely acts as an anode in weld sample, thus, the net current induced by κ phase is zero. In summary, the following relation is the expanded form of Eq. (13):

$$\overrightarrow{I}_{weld} + \overrightarrow{I}_{base} = \overleftarrow{I}_{weld} + \overleftarrow{I}_{base} \Rightarrow \overrightarrow{I}_{\beta'/weld} + \overrightarrow{I}_{\kappa/weld} + \overrightarrow{I}_{\beta'/base} = \overleftarrow{I}_{\alpha/weld} + \overleftarrow{I}_{\alpha/base} + \overleftarrow{I}_{\kappa/base} \tag{14}$$

The overall current measured by ZRA method, I_{couple}, is exactly the net current associated with the anode that flows toward cathode and that can be expressed as:

$$I_{couple} = \overrightarrow{I}_{weld} - \overleftarrow{I}_{weld} = \overrightarrow{I}_{\beta'/weld} + \overrightarrow{I}_{\kappa/weld} - \overleftarrow{I}_{\alpha/weld} \tag{15}$$

or, if it we assume that the galvanic current is the net current associated with the cathode that flows toward anode, then, it can be written as:

$$I_{couple} = \overleftarrow{I}_{base} - \overrightarrow{I}_{base} = \overleftarrow{I}_{\alpha/base} + \overleftarrow{I}_{\kappa/base} - \overrightarrow{I}_{\beta'/base} \tag{16}$$

In summary, the proposed model clearly demonstrates the origin of the galvanic current measured by ZRA method, which is also in agreement with potentiodynamic results. From microstructural point of view, the proportions of β′ and α were different in the base and weld samples, so the anodic current densities caused by β′, as well as cathodic current densities caused by α, of the base and weld samples were not similar. Moreover, the results indicated that the couple current is about few nanoamperes and hence, the gas tungsten arc welding procedure can be employed as a restorative and almost an invulnerable method for NAB joints.

4. Conclusions

In this research, corrosion of GTA welded nickel–aluminum bronze (C95800) is investigated by DC and AC electrochemical tests along with microscopic examinations. The microstructural and morphological modifications occurred during the welding operations in weld zone include a decrease in α phase, an increase in β′ phase and almost no changes in κ phase volume fractions. In addition, due to the higher volume fraction of β′ (the anodic phase) in the weld sample, it reveals anodic behavior. While, because of higher volume fraction of α (the cathodic phase) in base it behaves cathodic. Based on PDP and EIS results, the uniform corrosion resistance of instantly immersed weld and base regions are almost analogous and improved during immersion. At longer exposure times, the corrosion product layer grows and by slowing down the diffusion of reaction species through its porosities resulting in the alloy general corrosion resistance enhancement. Moreover, due to the better homogeneity of weld region, its surface layer discloses somewhat a better barrier characteristic after 72 h. On the other hand, since the major consequence of partial difference between volume fractions of the constituent phases is generation of a galvanic couple, ZRA results demonstrated that the couple current is only about a few nanoamperes. Therefore, it can be concluded that the general corrosion resistance of the restored damaged NAB parts could not be deteriorated in marine environments.

Acknowledgments

Ferdowsi University of Mashhad is appreciated for financial support and experimental facilities.

References

[1] Wharton JA, Barik RC, Kear G, Wood RJK, Stokes KR, Walsh FC. The corrosion of nickel–aluminium bronze in seawater. Corros Sci 2005;47:3336–67.
[2] Alfantazi AM, Ahmed TM, Tromans D. Corrosion behavior of copper alloys in chloride media. Mater Des 2009;30:2425–30.
[3] Schüssler A, Exner HE. The corrosion of nickel–aluminium bronzes in seawater – II. The corrosion mechanism in the presence of sulphide pollution. Corros Sci 1993;34(1803–11):13–5.
[4] Young-Gab C, Su-Il P, Chang-Ha K. Effect of aluminium content on the anodic behaviour of copper–aluminium alloys in 3.5 wt.% NaCl solution. Mater Lett 1994;20:265–70.
[5] Kear G, Barker BD, Stokes K, Walsh FC. Flow influenced electrochemical corrosion of nickel aluminium bronze – Part I. Cathodic polarisation. J Appl Electrochem 2004;34:1235–40.
[6] Kear G, Barker BD, Stokes K, Walsh FC. Flow influenced electrochemical corrosion of nickel aluminium bronze – Part II. Anodic polarisation and derivation of the mixed potential. J Appl Electrochem 2004;34:1241–8.
[7] Schüssler A, Exner HE. The corrosion of nickel–aluminium bronzes in seawater – I. Protective layer formation and the passivation mechanism. Corros Sci 1993;34:1793–802.
[8] Süry P, Oswald HR. On the corrosion behaviour of individual phases present in aluminium bronzes. Corros Sci 1972;12:77–90.
[9] Hyatt C, Magee K, Betancourt T. The effect of heat input on the microstructure and properties of nickel aluminum bronze laser clad with a consumable of composition Cu–9.0Al–4.6Ni–3.9Fe–1.2Mn. Metall Mater Trans A 1998;29:1677–90.
[10] Al-Hashem A, Riad W. The role of microstructure of nickel–aluminium–bronze alloy on its cavitation corrosion behavior in natural seawater. Mater Charact 2002;48:37–41.
[11] Fonlupt S, Bayle B, Delafosse D, Heuze J-L. Role of second phases in the stress corrosion cracking of a nickel–aluminium bronze in saline water. Corros Sci 2005;47:2792–806.
[12] Pidaparti RM, Aghazadeh BS, Whitfield A, Rao AS, Mercier GP. Classification of corrosion defects in NiAl bronze through image analysis. Corros Sci 2010;52:3661–6.
[13] Barik RC, Wharton JA, Wood RJK, Tan KS, Stokes KR. Erosion and erosion–corrosion performance of cast and thermally sprayed nickel–aluminium bronze. Wear. 259:230–42.
[14] Olszewski A. Dealloying of a nickel–aluminum bronze impeller. J Fail Anal Prev 2008;8:505–8.

[15] Wharton JA, Stokes KR. The influence of nickel–aluminium bronze microstructure and crevice solution on the initiation of crevice corrosion. Electrochim Acta 2008;53:2463–73.
[16] Fuller MD, Swaminathan S, Zhilyaev AP, McNelley TR. Microstructural transformations and mechanical properties of cast NiAl bronze: Effects of fusion welding and friction stir processing. Mater Sci Eng A 2007;463:128–37.
[17] Caron RN, Barth RG, Tyler DE. ASM Handbook, Metallography and Microstructures, vol. 9. ASM International; 2004.
[18] Oh-Ishi K, McNelley T. Microstructural modification of as-cast NiAl bronze by friction stir processing. Metall Mater Trans A 2004;35:2951–61.
[19] Oh-Ishi K, McNelley T. The influence of friction stir processing parameters on microstructure of as-cast NiAl bronze. Metall Mater Trans A 2005;36:1575–85.
[20] Kosec T, Milosev I, Pihlar B. Benzotriazole as an inhibitor of brass corrosion in chloride solution. Appl Surf Sci 2007;253:8863–73.
[21] Kear G, Barker BD, Walsh FC. Electrochemical corrosion of unalloyed copper in chloride media – a critical review. Corros Sci 2004;46:109–35.
[22] Babic R, Metikos-Hukovic M, Loncar M. Impedance and photoelectrochemical study of surface layers on Cu and Cu–10Ni in acetate solution containing benzotriazole. Electrochim Acta 1999;44:2413–21.
[23] Wood RJK, Hutton SP, Schiffrin DJ. Mass transfer effects of non-cavitating seawater on the corrosion of Cu and 70Cu–30Ni. Corros Sci 1990;30(1177–81):83–201.
[24] Yuan SJ, Pehkonen SO. Surface characterization and corrosion behavior of 70/30 Cu–Ni alloy in pristine and sulfide-containing simulated seawater. Corros Sci 2007;49:1276–304.
[25] Faita G, Fiori G, Salvadore D. Copper behaviour in acid and alkaline brines – I kinetics of anodic dissolution in 0.5M NaCl and free-corrosion rates in the presence of oxygen. Corros Sci 1975;15:383–92.
[26] Scendo M. Corrosion inhibition of copper by potassium ethyl xanthate in acidic chloride solutions. Corros Sci 2005;47:2778–91.
[27] Ni DR, Xiao BL, Ma ZY, Qiao YX, Zheng YG. Corrosion properties of friction-stir processed cast NiAl bronze. Corros Sci 2010;52:1610–7.
[28] Kear G, Barker BD, Stokes K, Walsh FC. Electrochemical corrosion behaviour of 90–10 Cu–Ni alloy in chloride-based electrolytes. J Appl Electrochem 2004;34:659–69.
[29] Wharton JA, Stokes KR. Analysis of nickel–aluminium bronze crevice solution chemistry using capillary electrophoresis. Electrochem Commun 2007;9:1035–40.
[30] Finsgar M, Lesar A, Kokalj A, Milosev I. A comparative electrochemical and quantum chemical calculation study of BTAH and BTAOH as copper corrosion inhibitors in near neutral chloride solution. Electrochim Acta 2008;53:8287–97.
[31] Huang H, Guo X, Zhang G, Dong Z. The effects of temperature and electric field on atmospheric corrosion behaviour of PCB-Cu under absorbed thin electrolyte layer. Corros Sci 2011;53:1700–7.
[32] Jiang T, Brisard GM. Determination of the kinetic parameters of oxygen reduction on copper using a rotating ring single crystal disk assembly (RRDCu(h k l)E). Electrochim Acta 2007;52:4487–96.
[33] Kear G, Barker BD, Stokes KR, Walsh FC. Corrosion and impressed current cathodic protection of copper-based materials using a bimetallic rotating cylinder electrode (BRCE). Corros Sci 2005;47:1694–705.
[34] King F, Quinn MJ, Litke CD. Oxygen reduction on copper in neutral NaCl solution. J Electroanal Chem 1995;385:45–55.
[35] De Sanchez SR, Schiffrin DJ. The flow corrosion mechanism of copper base alloys in sea water in the presence of sulphide contamination. Corros Sci 1982;22:585–607.
[36] Ijsseling FP. The application of the polarization resistance method to the study of the corrosion behaviour of CuNi10Fe in sea-water. Corros Sci 1974;14:97–110.
[37] Tan KS, Wharton JA, Wood RJK. Solid particle erosion–corrosion behaviour of a novel HVOF nickel aluminium bronze coating for marine applications-correlation between mass loss and electrochemical measurements. Wear 2005;258:629–40.
[38] Dermaj A, Hajjaji N, Joiret S, Rahmouni K, Srhiri A, Takenouti H, et al. Electrochemical and spectroscopic evidences of corrosion inhibition of bronze by a triazole derivative. Electrochim Acta 2007;52:4654–62.
[39] El-Sherif RM, Ismail KM, Badawy WA. Effect of Zn and Pb as alloying elements on the electrochemical behavior of brass in NaCl solutions. Electrochim Acta 2004;49:5139–50.
[40] Frignani A, Fonsati M, Monticelli C, Brunoro G. Influence of the alkyl chain on the protective effects of 1,2,3-benzotriazole towards copper corrosion. Part II: Formation and characterization of the protective films. Corros Sci 1999;41:1217–27.
[41] Ismail KM, Elsherif RM, Badawy WA. Effect of Zn and Pb contents on the electrochemical behavior of brass alloys in chloride-free neutral sulfate solutions. Electrochim Acta 2004;49:5151–60.
[42] Kosec T, Merl DK, Milosev I. Impedance and XPS study of benzotriazole films formed on copper, copper–zinc alloys and zinc in chloride solution. Corros Sci 2008;50:1987–97.
[43] Mountassir Z, Srhiri A. Electrochemical behaviour of Cu–40Zn in 3% NaCl solution polluted by sulphides: effect of aminotriazole. Corros Sci 2007;49:1350–61.
[44] Park C-G, Kim J-G, Chung Y-M, Han J-G, Ahn S-H, Lee C-H. A study on corrosion characterization of plasma oxidized 65/35 brass with various frequencies. Surf Coat Technol 2005;200:77–82.
[45] Rahmouni K, Keddam M, Srhiri A, Takenouti H. Corrosion of copper in 3% NaCl solution polluted by sulphide ions. Corros Sci 2005;47:3249–66.
[46] Ravichandran R, Rajendran N. Influence of benzotriazole derivatives on the dezincification of 65–35 brass in sodium chloride. Appl Surf Sci 2005;239:182–92.
[47] Trachli B, Keddam M, Takenouti H, Srhiri A. Protective effect of electropolymerized 3-amino 1,2,4-triazole towards corrosion of copper in 0.5 M NaCl. Corros Sci 2002;44:997–1008.
[48] Babic R, Metikos-Hukovic M. Spectroelectrochemical studies of protective surface films against copper corrosion. Thin Solid Films 2000;359:88–94.
[49] Hirschorn B, Orazem ME, Tribollet B, Vivier V, Frateur I, Musiani M. Determination of effective capacitance and film thickness from constant-phase-element parameters. Electrochim Acta 2010;55:6218–27.
[50] Idrac J, Mankowski G, Thompson G, Skeldon P, Kihn Y, Blanc C. Galvanic corrosion of aluminium–copper model alloys. Electrochim Acta 2007;52:7626–33.